GEOPHYSICS, VOL. 71, NO. 4 (JULY-AUGUST 2006); P. P29–P40, 14 FIGS.
10.1190/1.2213049

Robust estimates of 3D reflector dip and azimuth

Kurt J. Marfurt[1]

ABSTRACT

Much of seismic stratigraphy is based on the morphology of seismic textures. The identification of reflector terminations and subtle changes in dip and azimuth allows us to infer coherent progradational and transgressive packages as well as more chaotic slumps, fans, and braided-stream complexes; infill of karsted terrains; gas seeps; and, of course, faults and angular unconformities. A major difficulty in estimating reflector dip and azimuth arises at discrete lateral and vertical discontinuities across which reflector dip and azimuth change. The smearing across these boundaries produced by traditional dip and azimuth estimations is avoided by using temporally and spatially shifted multiple windows that contain each analysis point. This more robust estimation of dip and azimuth leads to increased resolution of well-established algorithms such as coherence, coherent amplitude gradients, and structurally oriented filtering. More promising still is the analysis of high-resolution dip and azimuth through volumetric estimates of reflector curvature and angular unconformities. This new technique is demonstrated using two land data volumes, one from the Louisiana salt province and the other from the fractured Fort Worth basin.

INTRODUCTION

After time-structure and amplitude-extraction maps, dip and azimuth maps of interpreted seismic reflectors are arguably the next most important product in interpretating 3D seismic data. Originally described by Dalley et al. (1989), dip and azimuth maps, along with closely related dip and azimuth shaded relief projections (Barnes, 2003), can highlight subtle faults having throws of less than 10 ms as well as stratigraphic features that manifest themselves through differential compaction or subtle changes in the seismic waveform. Lisle (1994) and Hart et al. (2002) show the relationship between reflector curvature and fracture density. Unfortunately, variability in reflector waveform and seismic noise can cause difficulties with attribute extractions made along picked horizons (Hesthammer and Fossen, 1997).

With recent advances in algorithm development, we can now calculate 3D cubes of reflector dip and azimuth without explicitly picking a given horizon. An early published work estimating dip directly from seismic data for interpretation purposes is by Picou and Utzmann (1962), who use a 2D unnormalized crosscorrelation scan over candidate dips on 2D seismic lines. Marfurt et al. (1998) generalize a later semblance-based scan by Finn (1986) to a true 3D scan. Barnes (1996, 2000a), presents an alternative approach based on 3D complex trace analysis originally applied to velocity analysis by Scheuer and Oldenberg (1988), while Bakker et al. (1999) present an estimate based on the gradient structure tensor.

No matter how we calculate dip and azimuth cubes, they can be a valuable interpretation tool. Currently, their most important use is to define a local reflector surface upon which we estimate some measure of discontinuity or, conversely, filter the data to extract its continuous component. Examples of the former include coherence and edge-detection measures (e.g., Luo et al., 1996; Marfurt et al., 1998; Gersztenkorn and Marfurt, 1999; Marfurt et al., 1999; Marfurt and Kirlin, 2000; Luo et al., 2001). Examples of the latter include conventional *f-x-y* deconvolution and structurally ordered filtering (Hoecker and Fehmers, 2002), also called edge-preserving smoothing (Bakker et al., 1999; Luo et al., 2002).

As a result of velocity distortions, estimates of reflector dip and azimuth from time-migrated seismic cubes are only loosely related to true dip and azimuth in depth. Even estimates calculated from prestack depth-migrated data suffer from errors in the background velocity model. Nevertheless, since dip and azimuth maps are differential rather than absolute measures of changes in reflector depth, they are less sensitive to long-wavelength errors in the velocity model than are reflector-depth measurements. Furthermore, most interpretations of dip and azimuth calculations are done on changes in dip and azimuth — either through color display (Marfurt et al., 1998; Lin et al., 2003), through visualization tools such as shaded relief projections (Barnes, 2003), or through explicit calculation of higher-order derivatives (Luo et al., 2001; Marfurt and Kirlin, 2000; al-Dossary and Marfurt, 2003) sensitive to reflector curvature or rotation.

Manuscript received by the Editor July 19, 2004; revised manuscript received November 14, 2005; published online August 1, 2006.
[1]University of Houston, Allied Geophysics Laboratories, Science and Research Building 1, Room 502F, Houston, Texas 77204. E-mail: kmarfurt@uh.edu.
© 2006 Society of Exploration Geophysicists. All rights reserved.

Barnes (2000b) has developed a suite of computer-generated textures similar to those used in traditional interpreter-driven seismic stratigraphy that measure reflector convergence, divergence, parallelism, and disorder — all based on an underlying estimate of dip and azimuth. For all of these reasons — for improved edge detection and structural filtering, as input to volumetric estimates of curvature, and as an interpretation attribute of value in its own right — improving our estimates of 3D reflector dip and azimuth is a worthwhile endeavor.

I begin my technical discussion by defining reflector vector dip in mathematical, geologic, and signal-analysis frameworks and review how estimates of reflector dip are made. I then present a way to improve these estimates by comparatively analyzing seismic reflector character in multiple temporally and spatially offset analysis windows, including each analysis point. Next, I present a new edge-preserving smoothing (EPS) algorithm obtained by projecting the data onto the principal-component eigenvector in the chosen window. Then I show how these improved estimates of vector dip and EPS significantly improve estimating coherence and coherent-amplitude gradients to highlight waveform and amplitude discontinuities. Finally, I show how these revised estimates of dip and azimuth improve estimates of reflector curvature, allowing interpreters to better visualize faults and unconformities, to visualize the interplay of faults and flexures, and to see subtle stratigraphic and diagenetic features.

BACKGROUND AND DEFINITIONS

Although geologists define the orientation of a geologic formation by its strike and dip, geophysicists prefer defining the orientation of seismic reflectors in terms of the inline and crossline apparent dips oriented along the axes of the seismic survey. In this section, we review these definitions along with the three most popular means of estimating vector dip of a seismic reflector: complex trace analysis, discrete vector dip scan, and gradient structure tensor.

Definition of reflector dip and azimuth

Mathematically, a planar element of a seismic reflector can be defined uniquely by a point in space, $\mathbf{x} = (x,y,z)$, and a unit normal to the surface, $\mathbf{n} = (n_x,n_y,n_z)$, where n_x, n_y, and n_z denote the components along the x-, y-, and z-axes, respectively, chosen such that $n_z \geq 0$ (Figure 1).

Geologically, we define a planar interface such as a formation top or internal bedding surface by means of the apparent dips θ_x and θ_y or, more commonly, by its true dip θ and its strike ψ (Figure 1). The apparent dip θ_x is the angle measured in the vertical (x,z) plane from the horizontal x-axis to the interface. Similarly, the apparent dip θ_y is the angle measured in the vertical (y,z) plane from the horizontal y-axis to the interface. The strike ψ is the angle between north (the y-axis in the SEG-Y trace header convention) and the intersection between the reflector and the horizontal (x,y) plane. The true dip θ is always greater than or equal to θ_x and θ_y and is the angle measured in a vertical plane perpendicular to the strike between the horizontal and the interface. Geologic dips are unsigned and are always measured downward from the horizontal to the surface. Since the strike defines a line (e.g., northeast-southwest) rather than a vector, we need to state, or more commonly post on a map, the direction of downward dip (e.g., northwest or southeast).

In reflection seismology, we avoid this mathematical ambiguity and commonly define a reflector by its dip and azimuth. The dip θ (more precisely called dip magnitude) is identical to that of the dip used in the geologic definition above. The azimuth ϕ (more precisely called dip azimuth) is measured either from the north or, for convenience, from the inline seismic survey axis. The azimuth is perpendicular to the geologic strike and is measured in the direction of maximum downward dip. In this paper, I use the reflection seismology notation of dip and azimuth, as well as apparent dips along the survey axes θ_x and θ_y, to define the reflector dip unit vector **a**, where

$$a_x = \cos\theta \cos\phi, \tag{1a}$$

$$a_y = \cos\theta \sin\phi, \tag{1b}$$

and

$$a_z = \sin\theta. \tag{1c}$$

Planar measurements — normal **n**, dip θ, strike ψ, apparent dips θ_x and θ_y, azimuth ϕ, vector dip **a** — are equivalent theoretically, but they can differ when stored with finite accuracy in an interpretation workstation. In particular, azimuth and strike are undefined for a horizontal reflector. In contrast, the reflector unit normal and its components are always defined. In the absence of knowing the velocity of the earth, it is often convenient to measure the apparent seismic (two-way) time dips p and q, where p is the apparent dip measured in s/m (or s/ft) in the inline or x-direction and q is the apparent dip measured in the same units in the crossline or y-direction. If the earth can be approximated by a constant velocity v, then the relationships between the apparent time dips p and q and the apparent angle dips θ_x and θ_y are

$$p = \frac{2\tan\theta_x}{v}, \tag{2a}$$

$$q = \frac{2\tan\theta_y}{v}. \tag{2b}$$

Calculation of vector dip using complex trace analysis

Luo et al. (1996) and Barnes (1996) describe a method of estimating vector dip based on a 3D extension of the analytic trace (or com-

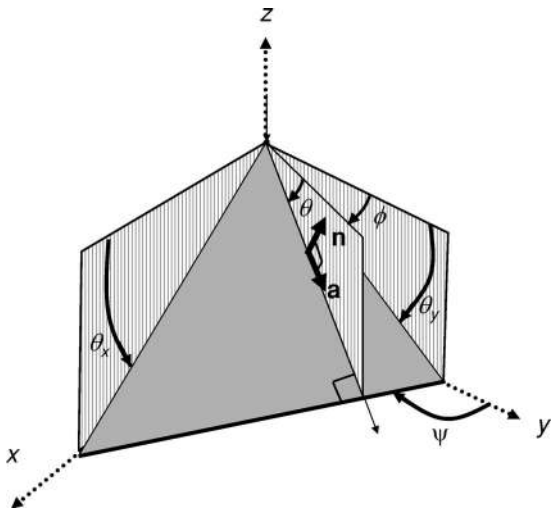

Figure 1. Mathematical, geological, and seismic nomenclature used in defining reflector dip: **n** is unit vector normal to the reflector, **a** is unit vector dip along the reflector, θ is dip magnitude, φ is dip azimuth, Ψ is strike, θ_x is apparent dip in the xz plane, and θ_y is apparent dip in the yz plane.

plex trace) attributes described by Taner et al. (1979). They begin with Taner et al.'s (1979) instantaneous frequency ω:

$$\omega(t,x,y) = \frac{\partial \Phi}{\partial t} = \frac{\partial}{\partial t}\text{ATAN2}(u^H,u) = \frac{u\dfrac{\partial u^H}{\partial t} - u^H\dfrac{\partial u}{\partial t}}{(u)^2 + (u^H)^2}, \tag{3}$$

where Φ denotes the instantaneous phase, $u(t,x,y)$ denotes the input seismic data, $u^H(t,x,y)$ denotes its Hilbert transform with respect to time t, and ATAN2 denotes the arctangent function whose output varies between $-\pi$ and $+\pi$. The derivatives of u and u^H are obtained either by using finite differences or via a Fourier transform, with the Fourier transform approach being particularly convenient since this is the domain in which the Hilbert transform typically is calculated.

The next step is to calculate the instantaneous wavenumbers k_x and k_y:

$$k_x(t,x,y) = \frac{\partial \Phi}{\partial x} = \frac{u\dfrac{\partial u^H}{\partial x} - u^H\dfrac{\partial u}{\partial x}}{(u)^2 + (u^H)^2} \tag{4a}$$

and

$$k_y(t,x,y) = \frac{\partial \Phi}{\partial y} = \frac{u\dfrac{\partial u^H}{\partial y} - u^H\dfrac{\partial u}{\partial y}}{(u)^2 + (u^H)^2}. \tag{4b}$$

The Hilbert transform can be calculated in any direction we choose. It may appear to be more consistent to apply the Hilbert transform along the x-axis for computating k_x and along the y-axis for k_y. However, since there is only one Hilbert transform for the data, we estimate it along the more densely sampled vertical time axis, or t-axis, where we encounter fewer artifacts from aliasing. For very large 3D input seismic data cubes, it is more convenient to estimate the spatial derivatives $\partial u/\partial x$, $\partial u^H/\partial x$, $\partial u/\partial y$, and $\partial u^H/\partial y$, using either central differences or a relatively short Fourier transform. This circumvents the need for keeping the entire data cube in memory or, alternatively, for transposing the cube prior to calculating the derivatives given in equation 4. The instantaneous time dip (p,q) is then obtained by calculating the ratio of k_x and k_y to ω:

$$p = k_x/\omega, \tag{5a}$$

$$q = k_y/\omega. \tag{5b}$$

The azimuth ϕ, measured from the y-axis, and true time dip s are given by

$$\phi = \text{ATAN2}(q,p) \tag{6a}$$

and

$$s = (p^2 + q^2)^{1/2}. \tag{6b}$$

If the input data are in the depth domain rather than in the time domain, we calculate k_z rather than ω:

$$k_z(z,x,y) = \frac{\partial \Phi}{\partial z} = \frac{u\dfrac{\partial u^H}{\partial z} - u^H\dfrac{\partial u}{\partial z}}{(u)^2 + (u^H)^2}, \tag{7}$$

where u^H is now the Hilbert transform with respect to depth z, allowing us to estimate angular dips θ_x and θ_y:

$$\theta_x = \tan^{-1}(k_x/k_z), \tag{8a}$$

$$\theta_y = \tan^{-1}(k_y/k_z), \tag{8b}$$

$$\theta = \tan^{-1}[(k_x^2 + k_y^2)^{1/2}/k_z], \tag{8c}$$

$$\phi = \text{ATAN2}(k_y,k_x). \tag{8d}$$

Figures 2a and 3a illustrate the seismic data, and Figures 2b and 3b

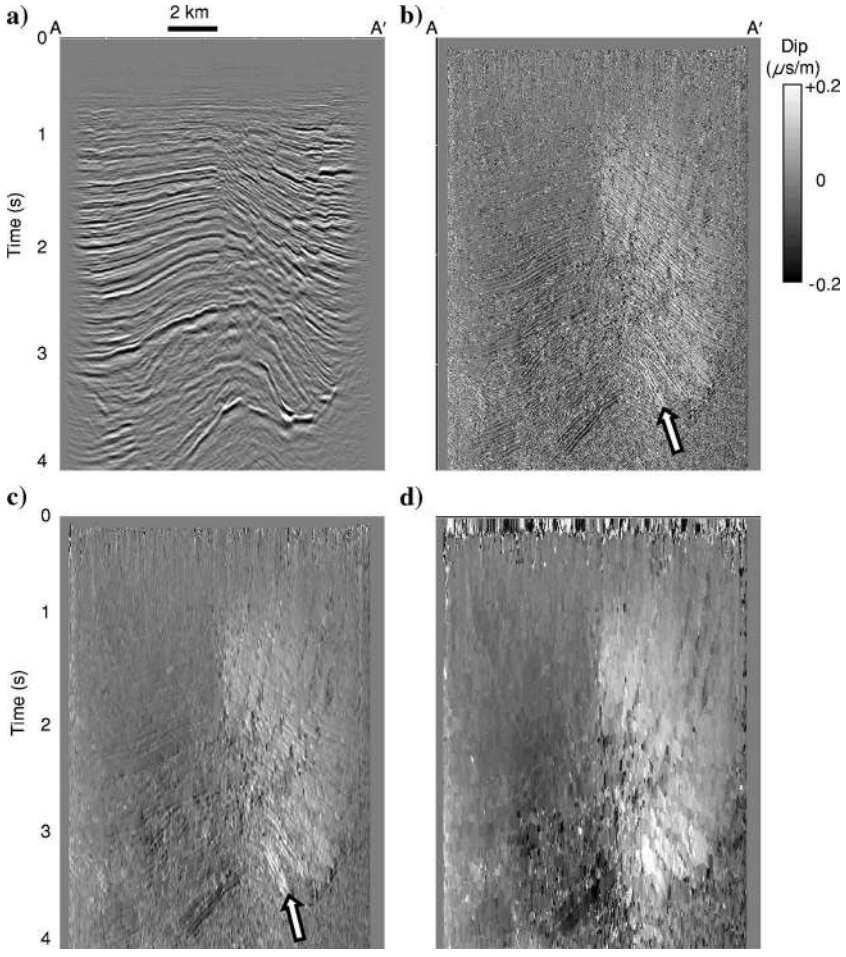

Figure 2. (a) Vertical slices along line AA' through the seismic data from a survey over Vinton Dome, Louisiana. The slices are through (a) the original seismic volume and through the east-west components. The apparent dip p, calculated using (b) the instantaneous dip estimation (equations 3, 4a, and 5a), (c) smoothed values of k_x and ω over a five-trace × five-trace × five-sample window, and (d) incorporating the multiwindow dip scan. Note the inconsistent estimate of interleaved positive and negative dips in (b), indicated by the white arrow, probably the result of singularities in the frequency and wavenumber calculations (Liner et al., 2004). This inconsistency is avoided by smoothing in (c) but at the cost of lateral resolution. The multiwindow dip scan is less sensitive to aliasing and honors the abrupt changes in dip seen along the faults. Data courtesy of OPEX.

exhibit the east-west component of instantaneous time dip p through a salt dome near Vinton, Louisiana.

Taner et al. (1979) warn that the estimate of instantaneous frequency given by equation 3 suffers from singularities when reflector events interfere with each other. Indeed, such singularities form the basis of the SPICE algorithm (Liner et al., 2004). To remedy this inaccuracy, Taner et al. (1979) suggest replacing equation 3 with an envelope-weighted average. Barnes (2000a) generalizes this concept to smoothing the calculation of ω, k_x, and k_y over 25 or more adjacent traces prior to estimating dip and azimuth, thereby improving stability with only minor loss of lateral resolution (Figures 2c and 3c). Even with such smoothing, the singularities in calculating ω, k_x, and k_y produce artifacts on the flanks of the dome.

Calculation of vector dip by discrete scans

Marfurt et al. (1998) generalize Finn's (1986) semblance scanning method to 3D data to generate a more robust means of estimating reflector dip (Figure 4):

$$s(\theta_x, \theta_y) = \frac{\sum_{k=K_S}^{K_E} \left\{ \left[\frac{1}{J} \sum_{j=1}^{J} u(k\Delta t - px_j - qy_j) \right]^2 + \left[\frac{1}{J} \sum_{j=1}^{J} u^H(k\Delta t - px_j - qy_j) \right]^2 \right\}}{\sum_{k=K_S}^{K_E} \left\{ \frac{1}{J} \sum_{j=1}^{J} [u(k\Delta t - px_j - qy_j)]^2 + \frac{1}{J} \sum_{j=1}^{J} [u^H(k\Delta t - px_j - qy_j)]^2 \right\}} \quad (9)$$

where p and q are given by equation 2, x_j and y_j denote the local coordinates of the jth trace measured from an origin at the analysis point, J denotes the total number of traces in the analysis window, and K_s and K_e denote the first and last temporal sample in the analysis window. Other amplitude-normalized measures include principal-component coherence (Gersztenkorn and Marfurt, 1999), lateral variance normalized by the energy, and least-squares fitting a plane to the data (Claerbout, 1992; Bednar, 1998). A disadvantage of dip-scan approaches is that they discretely sample θ_x and θ_y such that one may miss subtle features that might be discerned by the continuous complex trace analysis method given by equations 3–5 and 7.

Calculation of vector dip by the gradient structure tensor

The third method of estimating vector dip based on the gradient structure tensor is used by Bakker et al. (1999) and by Hoecker and Fehmers (2002) in their structure-oriented filtering work. They begin constructing their gradient structure tensor by computing the outer product of the gradient with itself (giving a symmetric 3×3 tensor of rank 1). The elements of this tensor are then smoothed individually by a low-pass spatial filter (typically by convolution in the spatial domain). This generates a positive (semi)definite 3×3 tensor with three eigenvectors. The eigenvector corresponding to the largest eigenvalue will by definition best represent the variability of the seismic data and therefore will be aligned with the vector normal to the structure (Bakker et al., 1999).

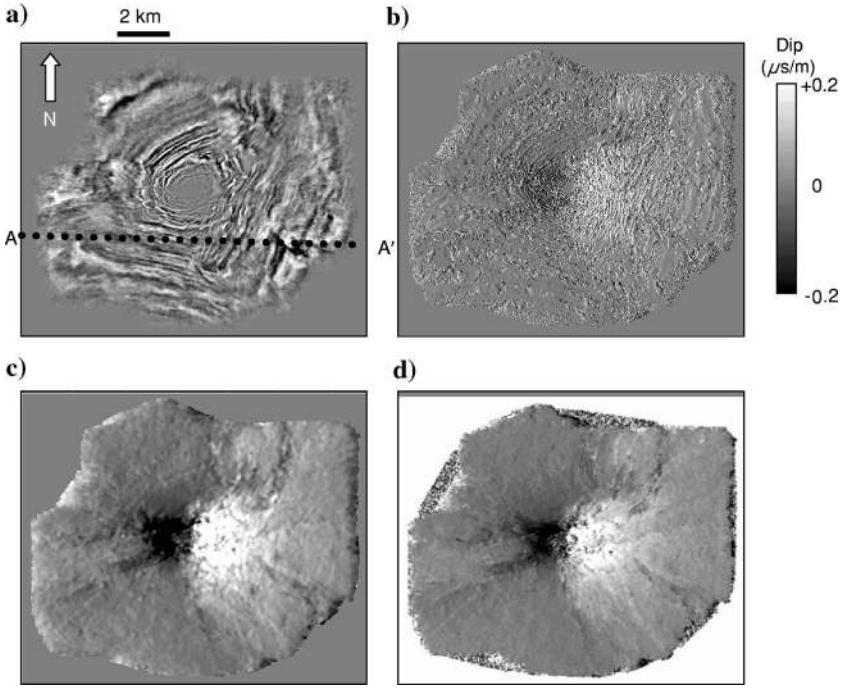

Figure 3. (a) Time slice at 1.0 s through the original seismic volume. Corresponding slice through the inline (east) components of apparent dip, calculated using (b) the instantaneous dip estimation (equations 3, 4a, and 5a), (c) smoothed values of k_x and ω over a five-trace $\times$ five-trace $\times$ five-sample window, and (d) incorporating the multiwindow dip scan. Note the aliasing at steep dips in (b). This aliasing is averted by smoothing in (c) but at the cost of decreased lateral resolution. The multiwindow dip scan method is less sensitive to aliasing and honors the abrupt changes in dip seen along the faults. Line AA' indicated on this image is shown in Figure 2.

Limitations of centered dip and azimuth estimations

Regardless of how these estimates of reflector dip are implemented, they all fail when the analysis window spans a fault, where they provide at best an estimate of the apparent dip across the fault rather than true reflector dip (Figure 5a). Such estimates of apparent dip across faults are excellent edge detectors (e.g., Luo et al., 1996). Smoothed estimates of the vector components of dip using mean or median filters can improve estimates of coherence (Marfurt et al., 1999) but at the expense of eliminating details of interest in the reflector dip volumes themselves.

METHOD

My improved method is based on a multiwindow dip-search algorithm that avoids smearing dip estimates across faults and angular unconformities. I show how these more accurate estimates of dip and azimuth provide better coherence estimates. We also show how we can apply principal component filters along these volumetric estimates of dip and azimuth to provide a structure-oriented filter. Finally, I show how lateral variations in these principal components provide attribute images that are mathematically independent of coherence, dip, and azimuth.

Robust estimates of 3D vector dip

Equation 9 provides values of semblance on a grid of discretely sampled angle pairs (θ_x, θ_y). I obtain an improved estimate of dip and azimuth by passing a 2D paraboloid through the nine discretely sampled points neighboring the point having the maximum semblance:

$$s(\theta_x, \theta_y) = \alpha_1\theta_x^2 + \alpha_2\theta_x\theta_y + \alpha_3\theta_y^2 + \alpha_4\theta_x + \alpha_5\theta_y + \alpha_6, \tag{10}$$

solving for the coefficients α_j in a least-squares sense. I then calculate an improved estimate of the vector dip by solving

$$\frac{\partial s(\theta_x, \theta_y)}{\partial \theta_x} = 2\alpha_1\hat{\theta}_x + \alpha_2\hat{\theta}_y + \alpha_4 = 0,$$
$$\frac{\partial s(\theta_x, \theta_y)}{\partial \theta_y} = \alpha_2\hat{\theta}_x + 2\alpha_3\hat{\theta}_y + \alpha_5 = 0 \tag{11}$$

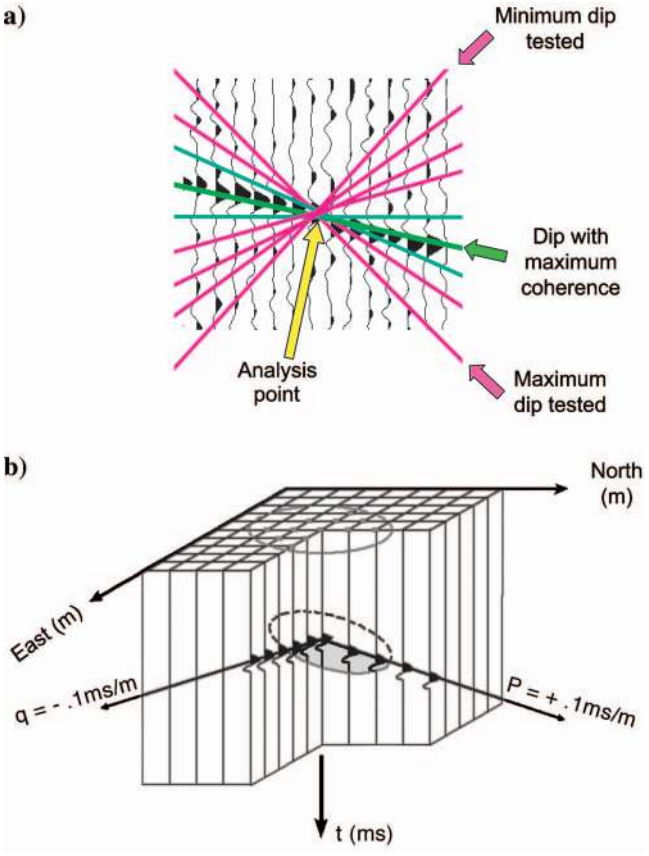

Figure 4. (a) Schematic showing a 2D search-based estimate of coherence. First, the algorithm estimates coherence using semblance, variance, principal component, or some other statistical measure (such as given by equation 9) along a discrete number of candidate dips shown as colored lines. In this example, the maximum coherence is calculated along the dip indicated by the green line. Next, the algorithm passes an interpolation curve through the coherence measures estimated by the peak value (along the green line) and through coherence measures along two or more neighboring dips (the cyan lines). The peak value of this curve estimates coherence, while the dip value of this peak estimates instantaneous dip. (b) A 3D search-based estimate of coherence; p indicates the inline and q the crossline components of vector time dip. The technique is analogous to that shown in (a) (after Marfurt et al., 1998).

for $(\hat{\theta}_x, \hat{\theta}_y)$, where $(\hat{\theta}_x, \hat{\theta}_y)$ is the apparent dip pair corresponding to the maximum of the interpolated semblance surface $s(\theta_x, \theta_y)$.

To improve the estimate of vector dip, I exploit the multiple-analysis-window construct described by Kuwahara et al. (1976) and generalized to seismic amplitudes by Luo et al. (2002) in their EPS algorithm. Luo et al. (2002) scan a suite of noncentered, overlapping analysis windows in addition to the centered window, all of which contain the analysis point of interest (Figure 6a). They then calculate the amplitude variance σ^2 over the J traces that fall within the ith window:

$$\sigma_i^2 = \frac{1}{J-1}\sum_{j=1}^{J}(u_{ji} - \langle u_i\rangle)^2, \tag{12}$$

where $\langle u_i\rangle$ denotes the average value of u_{ji} within the ith analysis window. The window with the smallest variance is assumed to best represent a coherent reflector and is used in subsequent EPS steps.

Since I expect the amplitudes themselves to change across a discontinuity, I use an energy-normalized coherence estimate (such as the semblance measure given by equation 9) rather than the nonnormalized variance given by equation 12. Although not explicitly stated by Luo et al. (2002), I need to search over a suite of candidate dips, using equations 9 and 10 to choose the window with the maximum coherence. Finally, I generalize the original concept of Luo et al. (2002) by also searching over candidate uncentered vertical analysis windows (Figure 6b) that include the analysis point.

Calculating a coherence measure over 45 overlapping nine-trace by eleven-sample windows generates the inline dip p shown in Figures 2d and 3d. Each window was scanned using 11 values of θ_x and 11 values of θ_y, or $11 \times 11 = 121$ dip and azimuth pairs, giving a total of 11 979 misfit calculations at each analysis point. The vector dip of the window with the maximum coherence is then assigned to the analysis point. By exploiting the fact that the overlapping windows can be reused for adjacent traces and samples, I reduce the total computation by two orders of magnitude. I processed the volume shown in Figure 2 consisting of 600 inlines, 660 crosslines, and 1500 samples on eight dual-CPU, 2-MHz nodes using the message passing interface (MPI) construct. Elapsed wall clock time for each iteration (three iterations of structurally oriented filtering) was 11.3 hours, the bulk of which (80%) appeared to be waiting on data transfer either to or from the master node. While the process may be sped up significantly with a faster programmer or speedier communication hardware, the important point is that the U. S. $16,000 hardware in-

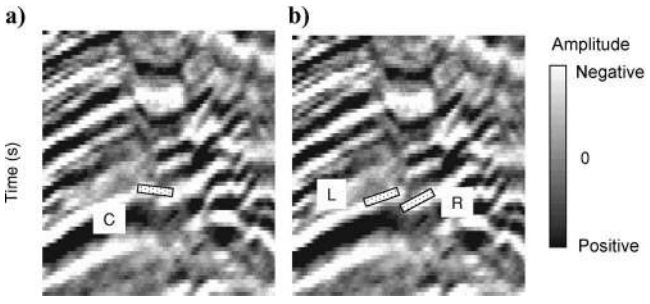

Figure 5. Schematic of the apparent dip (speckled line) estimated using the discrete search algorithm shown in Figure 4. (a) In a window C centered about the analysis point. (b) In windows L and R shifted to the right and left of the analysis point. Estimate of apparent dip obtained in either of these shifted windows is superior to the smoothed apparent dip given by the centered window.

vestment (2004 dollars) places such computation within the reach of even the smallest technology providers.

Impact of robust reflector dip estimates on coherence estimates of reflector discontinuities

Bakker et al. (1999) note that the Kuwahara et al. (1976) algorithm can produce patchy images and suggest favoring the centered analysis window when dealing with noisy data. I do so by modifying the semblance s^{cent} (or other coherence measure) at the centered analysis window to be

$$s^{\text{cent}}_{\text{new}} = as^{\text{cent}} + b, \tag{13}$$

where $a \geq 1$ and $b \geq 1$. Values of $a = 1$ and $b = 0$ reproduce Kuwahara's et al. (1976) original algorithm, while a value of $b = 1.0$ will force a centered, single-window algorithm. A value of $a = 1.02$ and $b = 0.1$ works well for good-quality land data such as shown in this paper.

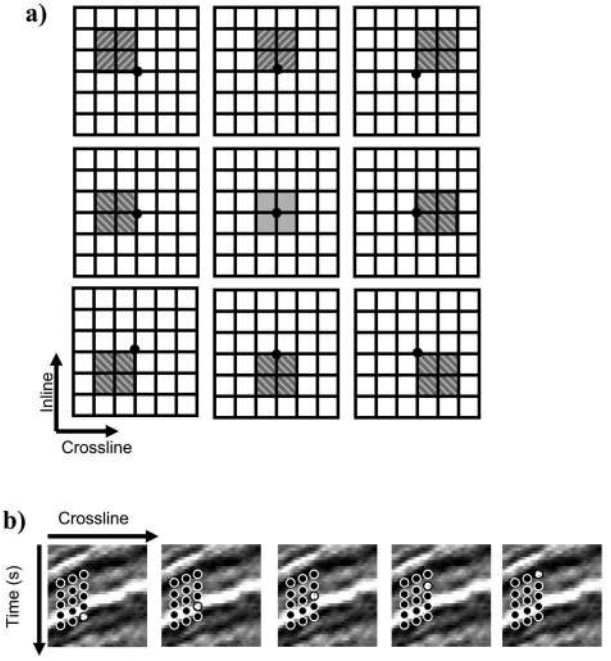

Figure 6. (a) Plan view of a nine-trace, nine-lateral-window search for dip and azimuth. Solid circles indicate the analysis point; shaded rectangles indicate alternative analysis windows. (b) Vertical view of the first (northwest) window shown in (a), illustrating the search over five vertical windows containing the analysis point indicated by the speckled dot (only the three crossline traces and five vertical samples of the 3D analysis window are displayed). First, the coherence, dip, and azimuth within each window are calculated and then interpolated for (see Figure 4). This process is repeated for the nine laterally shifted by five temporally shifted analysis windows, resulting in 45 overlapping analysis windows — each containing the desired analysis point. The dip and azimuth at the analysis point are defined to be the dip and azimuth of the window encompassing the analysis point which has the maximum coherence. The use of such temporally and laterally shifted analysis windows helps preserve angular unconformities and other features of geologic interest. This dip and azimuth and the traces comprising the most coherent window are used for the covariance matrix and principal-component data projection calculations (equations 14 and 15).

Let's return to Figure 5, which displays a seismic section consisting of dipping reflectors cut by a fault. For a sample in the fault zone, the maximum coherence value in a centered window *c* would give an erroneous apparent dip across the fault as shown in Figure 5a. In contrast, dip estimates using a left-shifted window *L* or right-shifted window *R* accurately project true dip on either side of the fault (Figure 5b). Choosing the dip corresponding to the maximum coherence in the centered analysis window results in an image of reduced contrast, with the amount of contrast dependent on the relative displacement and/or realignment with deeper or shallower reflectors across the fault.

Marfurt et al. (1999) address this problem by calculating coherence along a (mean or median) filtered version of the reflector vector dip in each time slice. Such smoothing works well when the reflector dip is similar on either side of the fault. However, if the reflectors are rotated with respect to each other across the fault, the filtered estimate may be incorrect. The more robust estimate of reflector dip and azimuth obtained using the multiple-window search algorithm described in this paper preserves reflector vector dip in the presence of faults and thereby circumvents the need to perform additional smoothing.

Principal-component filtering

Having estimated the reflector dip in the analysis window containing the analysis point of interest which has the maximum coherence, I next estimate a filtered version of the data that avoids smoothing over structural and stratigraphic edges. Luo et al. (2002) replace the amplitude of the analysis point with the mean value of samples extracted from the neighboring traces within the selected window aligned with the dipping reflector. As a variation of this approach, I could calculate the median or α-trim mean in lieu of the mean. A problem arises for fractures that often appear as discrete, narrow lineaments having higher or lower amplitude than the neighboring traces. Applying a mean or median filter to such lineaments may eliminate them. Done (1999) describes using principal components to estimate and then filter out backscattered ground roll. In my application, if *m* is the analysis point in the laterally shifted Kuwahara window, the principal-component-filtered data are given by

$$u^1_m(t) = \left[\sum_{j=1}^{J} u_j(t)v^1_j(t)\right] v^1_m(t), \tag{14}$$

where $\mathbf{v}^1(t)$ is the first eigenvector (the vector that best represents the lateral amplitude variation across the *J* traces in the analysis window) corresponding to the covariance matrix **C**:

$$C_{ij}(t) = \sum_{k=K_s}^{K_e} [u_i(k\Delta t + px_i - qy_i)u_j(k\Delta t + px_j - qy_j) + u^H_i(k\Delta t + px_i - qy_i)u^H_j(k\Delta t + px_j - qy_j)]. \tag{15}$$

Here, *i* and *j* are trace indices in the laterally shifted Kuwahara window (Figure 6a), x_i and y_i (x_j and y_j) are the distances along the *x*- and *y*-axes of the *i*th (*j*th) trace from the analysis point, and the time samples between K_s and K_e straddle the analysis point (Figure 6b). I use the Hilbert transform of the data as an additional sample vector when calculating a real-valued covariance matrix rather than form a complex-valued Hermitian symmetric covariance matrix from the ana-

lytic trace. Using the data and its Hilbert transform avoids unstable estimates of the covariance matrix for small vertical windows centered about a trace zero crossing. Using a complex-valued Hermitian symmetric covariance matrix (and corresponding complex principal components) provides some extra, uncontrolled phase rotation beyond that provided by the dip search and interpolation, and it results in images that have somewhat lower lateral resolution and noise rejection. The covariance matrix calculation given by equation 15 differs from that used by Gersztenkorn and Marfurt (1999) and Marfurt et al. (1999) in that I use the Hilbert transform of the input data in addition to the input data itself and that, in general, the window is temporally and laterally shifted from rather than centered about the analysis point.

The behavior of Luo et al.'s (2002) EPS filter and the principal-component projection given by equation 14 are quite different. Both filters suppress random noise. Both filters also reject coherent noise cutting across the strongest reflector in the window, such as backscattered surface waves. Unfortunately, they can also eliminate desirable crosscutting signals, such as mismigrated fault-plane reflections. Luo et al. (2002) show how the edge-preserving mean filter can suppress the acquisition footprint. If the acquisition footprint comes from leakage of side-scattered noise, then the principal component filter reduces the footprint better. However, the acquisition footprint can also be a function of signal variability from differences in fold, source-receiver offset, and source-receiver azimuth between adjacent bins. Such differences are particularly sensitive to errors in velocity-induced NMO errors (Hill et al., 1999). In this case where the footprint pattern is slowly varying in the vertical direction, the principal-component filter will preserve and even enhance the acquisition footprint, while a mean or median filter will suppress it. Fractures that are nearly vertical are nearly indistinguishable from this kind of acquisition footprint. Since I am interested in mapping fractures, I use the principal-component filter and accept some image contamination from the acquisition footprint.

Recursive application of principal-component filtering

Once an edge-preserving filtered version of the data is generated, I can use it recursively as input to a second analysis, where I recalculate vector dip, coherence, amplitude gradients, and a second pass of filtering, if desired. For particularly noisy data, such as land data, we can greatly accelerate the interpretation process by using autopickers on the smoothed data, as recommended by Hoecker and Fehmers (2002). These picks on the smoothed data can then be transferred to the more difficult-to-pick original data by snapping the smoothed picks to peaks or troughs of previous versions of the data. I plot the data corresponding to line AA' in Figure 2a on the face of a folded image before and after two applications of principal-component EPS in Figures 7a and b. In Figures 7c and d I plot the corresponding vertical slice through the coherence volume. In all of Figure 7 I plot the coherence slice at 1.0 s folded over at line AA'. While the reflector terminations are clearly preserved and random noise is reduced, the reflector terminations interfinger. This interfingering is from an incorrect velocity used in the migration and cannot be repaired by any postmigration image processing algorithms (Duncan et al., 2002).

Coherent amplitude gradients

Once I have calculated the principal-component eigenvector $\mathbf{v}^1(t)$, I can estimate the reflection energy variation both parallel and perpendicular to the reflector. I illustrate this concept for an idealized

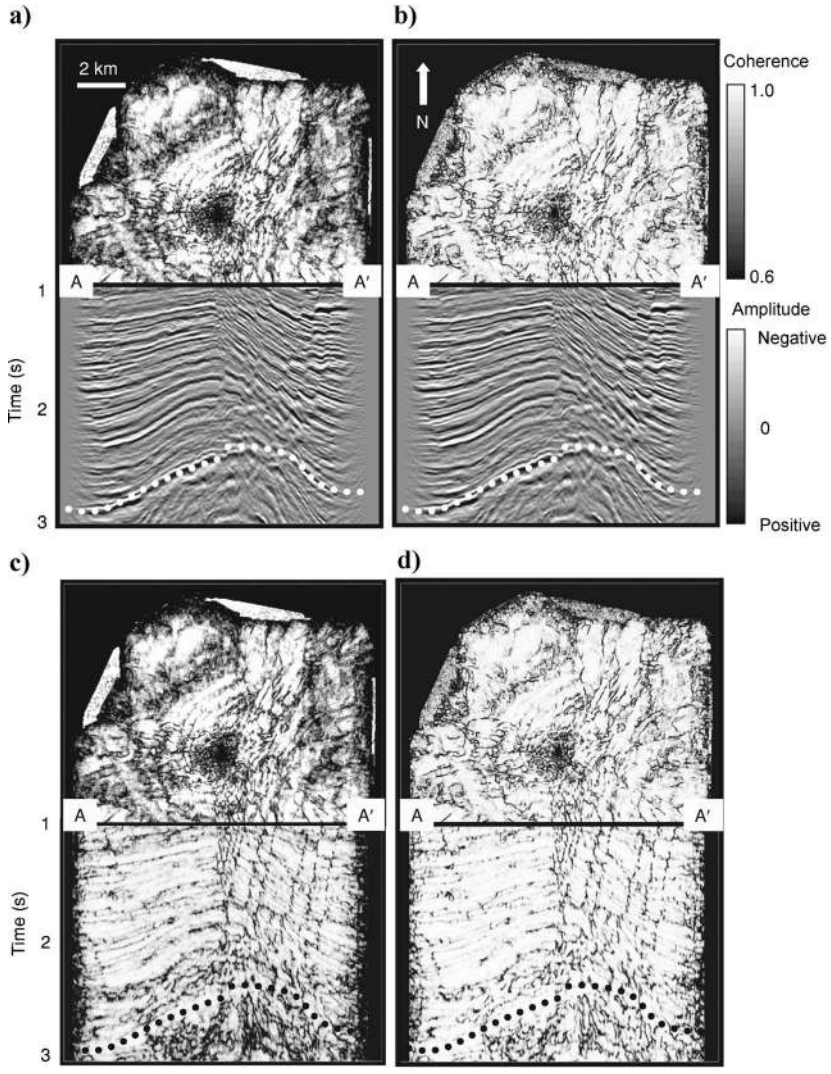

Figure 7. Foldaway images of the principal-component coherence time slice at t = 1.0 s and corresponding vertical slice through the seismic data along AA'. (a) The single-window search method (Marfurt et al., 1998) described in Figure 4. (b) The multiwindow search of reflector dip and azimuth along with principal-component filtering of the seismic data. The second algorithm sharpens faults, thereby enhancing coherence. The dotted line indicates the top of the Hackberry Formation discussed in Figure 10. (c) and (d) Foldaway images, the result of the single-window and multiwindow search of reflector dip and azimuth, with coherence plotted on the vertical slice.

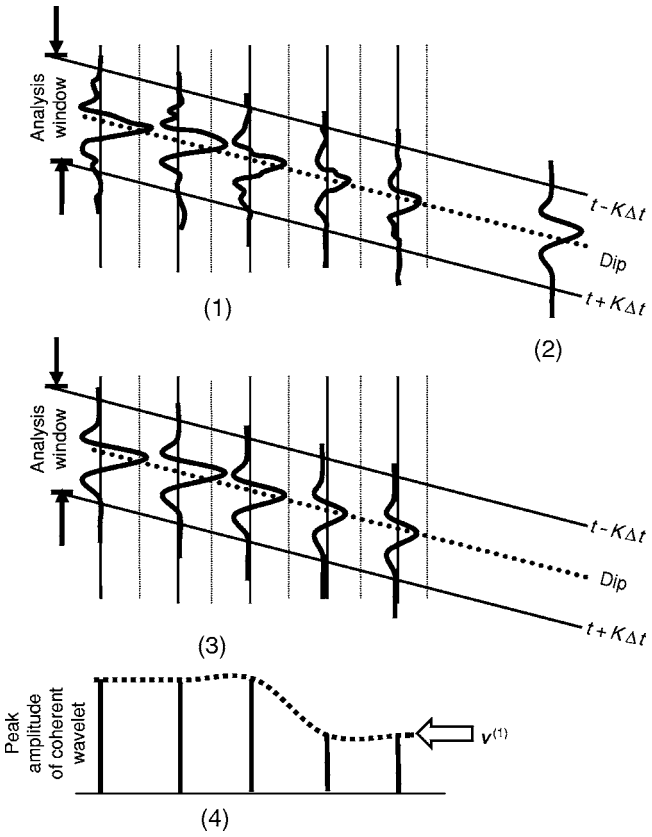

Figure 8. Schematic summarizing the steps in principal-component filtering and in computing the coherent energy gradient. (1) Calculate the energy of the input traces within an analysis window. (2) Calculate the single seismic waveform that best approximates the waveform of each input trace. (3) Replace each trace by a scaled version of step 2 that best fits each input trace. The amplitudes of the five wavelets in step 3 define the components of the five-element-long principal-component eigenvector $\mathbf{v}^{(1)}$. To calculate coherent-amplitude, energy-weighted gradients, take the derivative of the dotted curve in step 4 and weigh it by the sum of the coherent energy within the analysis window in step 3.

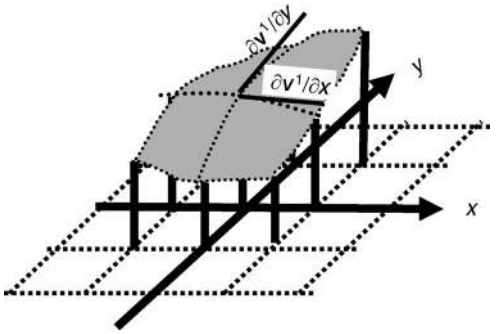

Figure 9. Interpretation of the eigenvector $\mathbf{v}^1$ corresponding to a nine-trace analysis window as the representation of a map of coherent amplitude $v(x,y)$. From this map one can calculate gradients $\partial v/\partial x(x,y)$ and $\partial v/\partial y(x,y)$, which indicate lateral changes in coherent amplitude. These gradients are particularly useful in mapping lateral changes in bed thickness below one-fourth wavelength tuning, where the amplitude is proportional to thickness and the waveform is nearly constant.

2D analysis in Figure 8. The principal component of the seismic data can be interpreted as a single waveform (Figure 8b) that best fits the input seismic data within an analysis window (Figure 8a). While the waveform has a fixed shape, its amplitude in general will vary laterally within the analysis window (Figure 8c). These amplitudes form the (length = 5) first eigenvector $\mathbf{v}^1(t)$, shown in Figure 8d. The eigenvector has five elements, one corresponding to each trace.

For 3D data, I interpret the mathematical eigenvector $\mathbf{v}^1(t)$ as a discretely sampled map $v(x,y)$ that represents the lateral variation of the coherent energy about the analysis point (Figure 9). Since I want to accentuate both lateral and vertical discontinuities, I use a window centered about the analysis point but whose dip and azimuth were calculated from the laterally and temporally shifted window having the maximum coherence.

Marfurt and Kirlin (2000) calculate such gradients as a byproduct of using a (lower-resolution) frequency-domain coherence algorithm. There are two variations of the amplitude gradient calculation. The simpler estimate is applied to the unit length principal-component eigenvectors themselves, $\mathbf{v}^1$. Its derivatives are called eigenvector gradients. Unfortunately, such gradients are overly sensitive to noise in low-energy areas of the seismic volume. A more useful estimate weights these derivatives by the principal-component eigenvalue λ_1. If we recall that

$$\mathbf{C}\mathbf{v}^1 = \lambda_1 \mathbf{v}^1 \tag{16}$$

and assume for simplicity that the seismic waveform is completely coherent (fit by only one eigenvector), we recognize that each diagonal element of $\mathbf{C}$ is a measure of energy based on the real and quadrature parts of the seismic traces. Then λ_1 is a measure of the total energy within the analysis window, while $\mathbf{v}^1$ is a measure of the lateral variation of amplitude across the analysis window. I therefore call the spatial derivatives of $\lambda_1\mathbf{v}^1$ coherent energy-weighted amplitude gradients. The coherent energy-weighted amplitude gradients are large when there is rapidly varying high-amplitude coherent energy and small when the reflectivity is either smoothly varying, low energy, or incoherent. These coherent energy-weighted amplitude gradient images are quite complementary to coherence images and provide needed detail in reservoirs represented by a strong, consistent reflection.

Although initially I used a finite-difference approximation along the inline and crossline axes to calculate these derivatives, I have found that the images sometimes have a different sensitivity to noise than those taken using a diagonal $(+45°,-45°)$ finite-difference operator. Furthermore, conventional finite-difference operators do not appear to use all of the information within the analysis window. So I define my derivatives of the eigenvector $\mathbf{v}$ evaluated at $J-1$ points within an analysis window to be

$$\frac{\partial v}{\partial x}(x,y) \approx \frac{2}{J-1}\sum_{j=2}^{J}\frac{x_j}{2r_j^2}v_j, \tag{17a}$$

$$\frac{\partial v}{\partial y}(x,y) = \frac{2}{J-1}\sum_{j=2}^{J}\frac{y_j}{2r_j^2}v_j, \tag{17b}$$

where

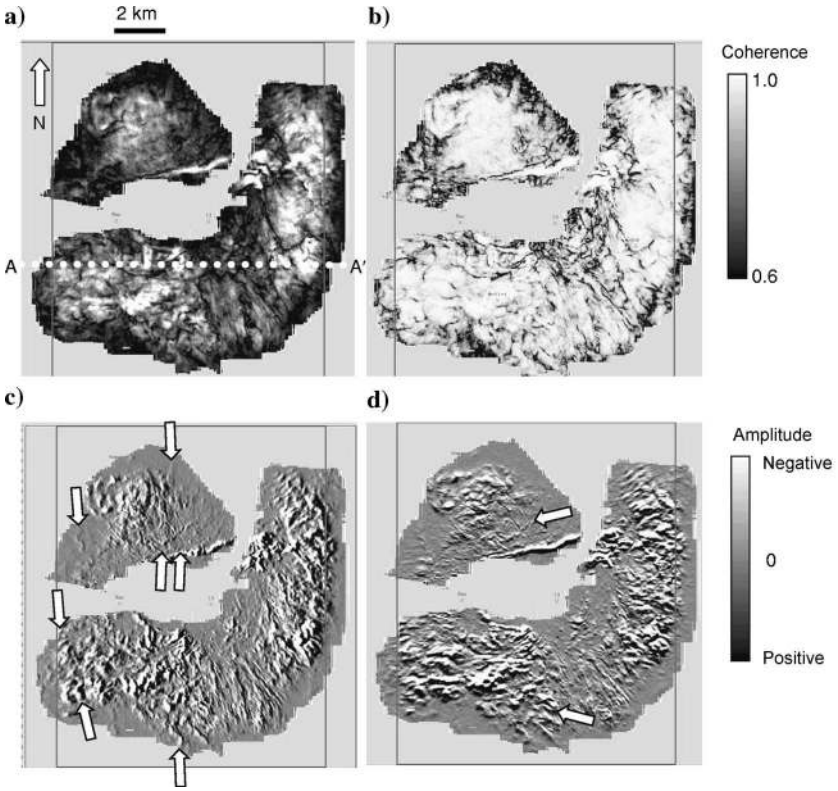

Figure 10. (a) Amplitude, (b) coherence, (c) east-west coherent energy-weighted amplitude gradient, and (d) north-south coherent energy-weighted amplitude gradient extractions along the Hackberry horizon shown in Figure 7. Faults have a wormy appearance because the data have been poorly migrated, resulting in interfingering of reflectors. In contrast, the energy-weighted amplitude gradients away from the faults give accurate images of channels (indicated by arrows) and other stratigraphic features, including areas where the coherence is very high (white). (Seismic data courtesy of OPEX).

$$r_j = (x_j^2 + y_j^2)^{1/2}. \qquad (17c)$$

The analysis point at the center of the window is omitted from the calculation. Inspection of these formulas shows that they can be interpreted as an unweighted average of x- and y-components of directional derivatives obtained by pairs of points straddling the analysis point in the analysis window.

Although gradients of coherent energy can be quite effective in mapping faults and fractures, I have found them to be most useful in delineating thin channels where they emphasize subtle lateral changes in tuning. Stratigraphic features are best examined using horizon slices that better represent a fixed point in geologic time. Figure 10 displays slices along the Hackberry horizon through volumes of the original seismic amplitude and coherence, as well as the east-west and north-south components of the coherent amplitude gradient. Because of the complex lateral variation in velocity and the use of prestack time versus prestack depth migration, the resolution of the coherence images is inferior to those at the shallower 1-s level (Figure 7). However, one can still clearly identify meandering channels that formed before and during salt diapirism. Identification of such channels in a structural setting can offer interesting exploration opportunities.

APPLICATION

Figure 11 displays a vertical seismic line BB' before and after structurally oriented principal-component filtering through a merged land survey acquired in the Fort Worth basin, Texas. Random noise, primarily from backscattered surface waves entering the stack and migration, are suppressed, while lateral and vertical discontinuities are preserved. Figure 12 displays the time-struc-

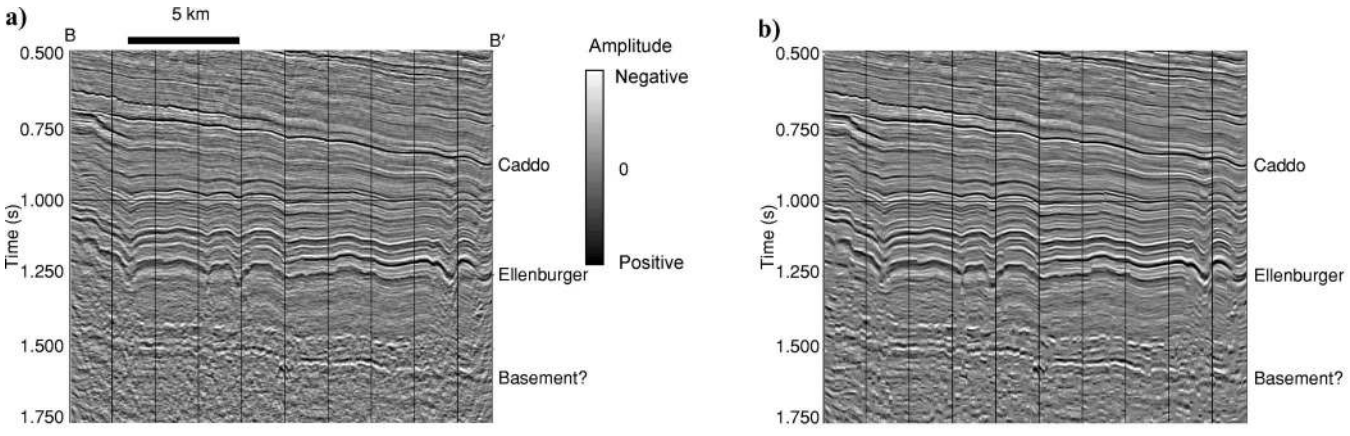

Figure 11. Line BB' through a Fort Worth basin survey (a) before and (b) after two passes of principal-component structurally oriented filtering using equation 14 and the multiwindow approach described in this paper. Nine overlapping nine-trace windows and eleven vertical windows (± 10 ms) were used. Random noise, primarily from backscattered ground roll entering the migration and stack, is suppressed, while lateral discontinuities are well preserved. (Seismic data courtesy of Devon Energy.)

ture and amplitude-extraction maps along the Pennsylvanian-age Caddo Limestone horizon, chosen because it has the highest S/N level of any horizon in the survey. We are able to see clearly the different levels of data quality of the three merged surveys in Figure 13b. In Figure 12b, the mean curvature, defined by Roberts (2001) for nearly horizontal reflectors, is

$$k_{\text{mean}} = \frac{1}{2}\left(\frac{\partial^2 t}{\partial x^2} + \frac{\partial^2 t}{\partial y^2}\right), \tag{18a}$$

while Figure 13b illustrates the calculated mean curvature using multiwindow estimates of inline and crossline dip using the equivalent formula.

$$k_{\text{mean}} = \frac{1}{2}\left(\frac{\partial p}{\partial x} + \frac{\partial q}{\partial y}\right). \tag{18b}$$

By using these more robust estimates of dip and azimuth, we can track lineations (white arrows) and collapse features (black arrows) into the two surveys of reduced data quality. Note that the lateral resolution provided by this robust estimate of reflector dip is equivalent to that provided by carefully picking reflector times on a reflector having good S/N ratio.

To demonstrate that these calculations have been performed on a volume rather than on horizons, I display a time slice at 0.8 s through the coherence and most negative curvature volumes in Figure 14. The most positive and most negative curvature [see Roberts (2001) for a complete definition] are frame-invariant measures of the two principal radii of curvature that fit a quadratic surface. The coherence and vector dip calculations both used a nine-trace by eleven-sample (±10 ms) analysis window, with the coherence calculated along the same reflector dip used in the curvature calculation. We note considerable detail of fractures and collapse features on the most negative curvature slice that is not seen on the coherence slice. The reason for this difference is geologic rather than algorithmic: the two attributes measure independent features (waveform similarity versus reflector morphology) of the seismic reflection event. Work by al-Dossary and Marfurt (2003) provides a more detailed description of volumetric curvature calculations (at different wavelengths or spectral scales), and Sullivan et al. (2003) provide a detailed ex-

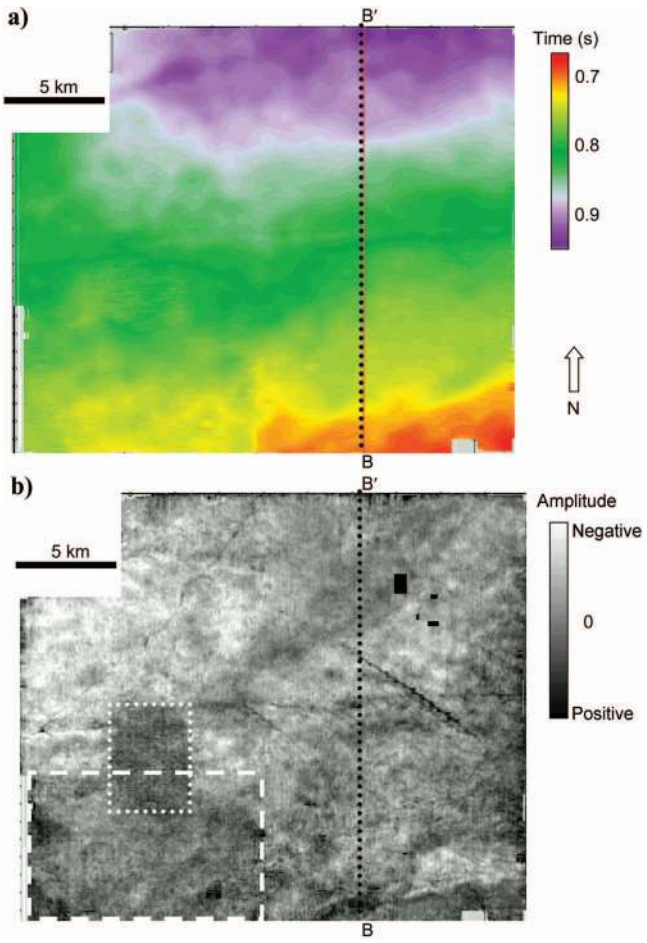

Figure 12. (a) Time- structure and (b) amplitude-extraction map corresponding to the Caddo horizon shown in Figure 11. The survey indicated by the dotted rectangle was acquired in 1993, that by the dashed rectangle was in 1995, and the remainder was in 1997. The same contractor reprocessed all three surveys in 1999, such that the differences in data quality reflected advances in acquisition design rather than in processing.

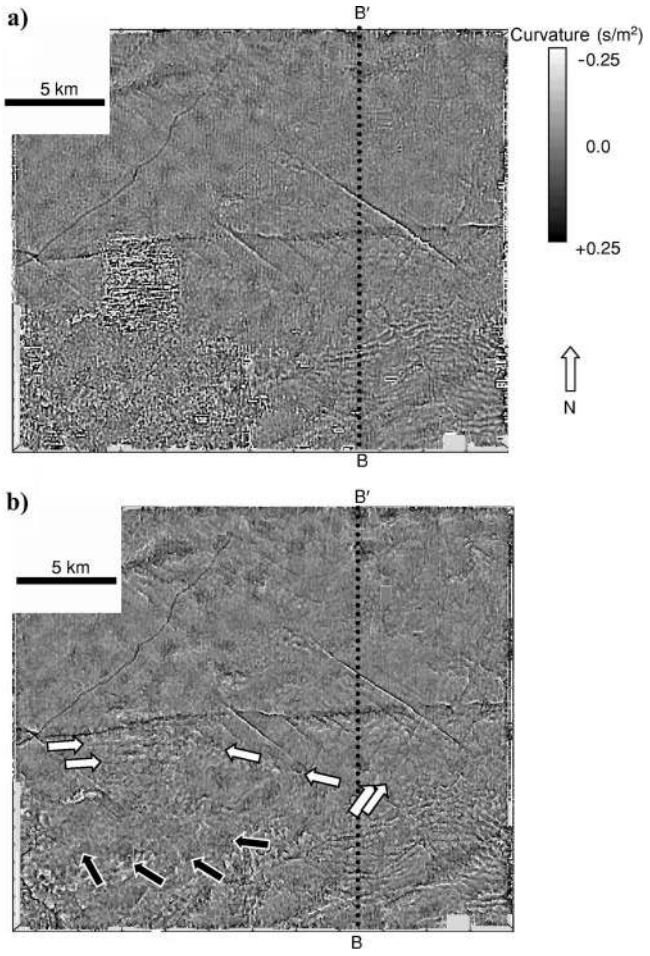

Figure 13. (a) Horizon slice along the Caddo horizon of mean curvature k_{mean} from the time picks $t(x,y)$ shown in Figure 12a, using equation 18a. (b) Estimates of p and q using the multiwindow dip search technique described and equation 18b. White arrows indicate lineaments; black arrows collapse features not readily seen on the conventional curvature calculations shown in (a). The difference is most pronounced in the southwest, where we encounter the older surveys with lower S/N ratios.

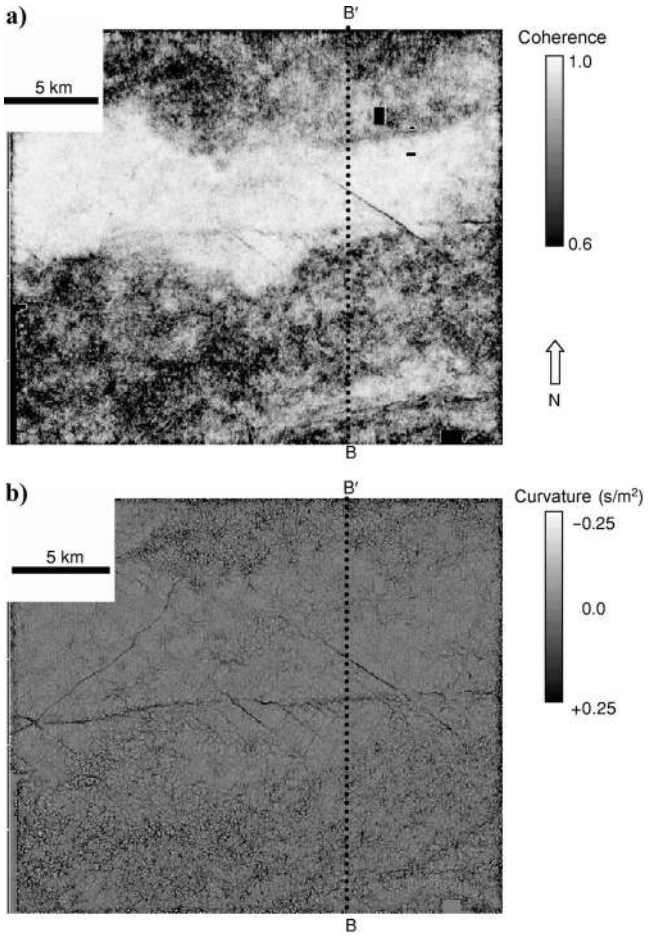

Figure 14. Time slice at 0.8 s through the (a) coherence and (b) most negative curvature volumes at approximately the Caddo horizon shown in Figures 12 and 13. Note that coherence shows an east-west strike-slip fault and a few northwest-southeast tension gashes. In contrast, the most negative curvature volume, based on the estimates of the vector dip components p and q, show considerable detail of a system of complex joints and fractures. Unlike horizon-based attributes, a robust estimate of vector dip allows us to generate curvature attributes throughout the entire survey volume.

planation of the geologic interpretation of this fractured and karsted terrain.

CONCLUSIONS

I have introduced a dip and azimuth computation that avoids smearing across faults, angular unconformities, and other discontinuities through a nonlinear dip search over a suite of overlapping windows. Through careful implementation and reuse of coherence calculations within each window used, the cost of the algorithm is nearly identical to that of commonly used single-window dip search algorithms. In its current implementation, the cost of recursive use of the algorithm for EPS is proportional to the number of recursions run (i.e., a factor of two or three).

Accurate estimates of reflector dip and azimuth (or vector dip) are the fundamental building blocks for all geometric attributes as well as for structurally oriented filtering. Coherence calculations along accurate estimates of dip have higher lateral resolution and are less sensitive to structural folding and warping overprints than coherence calculations performed when the vector dip is ignored or somehow smeared. Short-wavelength spectral components of reflector curvature (al-Dossary and Marfurt, 2003), which are derivatives of vector dip, exhibit improved lateral resolution. Not surprisingly, long-wavelength spectral components of curvature are less sensitive to high-resolution estimates of vector dip. These new volumetric calculations appear to be quite effective in delineating folds, fractures, karsts, slumps, and differential compaction (Blumentritt et al., 2003; Sullivan et al., 2003). Although not shown by the examples in this paper, vertical changes in vector dip and curvature are good candidates for mapping unconformities. Coherent-amplitude gradients calculated along vector dip appear to delineate channels and other subtle stratigraphic features that are expressed as lateral changes in thin-bed tuning.

By using vector dip as input for principal-component filtering in the most coherent window containing each analysis point, we can enhance lateral resolution and reduce both random and coherent noise.

ACKNOWLEDGMENTS

This paper has been improved significantly by the careful critiques of two anonymous reviewers. The author acknowledges and thanks the U. S. Department of Energy for its support during the period when this work was performed as part of grant DE-FC26-01BC15353, focused on the geophysical analysis of Vinton Dome, Louisiana. The author also is indebted to his colleagues at Allied Geophysics Laboratories — Peter Bartok, Chuck Blumentritt, Al Lacazette, Charlotte Sullivan, and Isabel Serrano — for their encouragement and extensive work in attribute calibration. Saleh al-Dossary and Cory Hoelting inspired and served as sounding boards for ideas in algorithm development. Thanks to the reviewers for constructive feedback and particularly to Gijs Fehmers for clarifying the construction of the gradient structure tensor. Finally, the author thanks OPEX and Devon Energy for the use of their data.

REFERENCES

al-Dossary, S., and K. J. Marfurt, 2003, Improved 3D seismic edge detection filter applied to Vinton Dome, Louisiana: 73rd Annual International Meeting, SEG, Expanded Abstracts, 2370–2372.

Bakker, P., L. J. van Vliet, and P. W. Verbeek, 1999, Edge-preserving orientation adaptive filtering: Conference on Computer Vision and Pattern Recognition, IEEE-CS, Proceedings, 535–540.

Barnes, A. E., 1996, Theory of two-dimensional complex seismic trace analysis: Geophysics, **61**, 264–272.

———, 2000a, Weighted average seismic attributes: Geophysics, **65**, 275–285.

———, 2000b, Attributes for automated seismic facies analysis: 70th Annual International Meeting, SEG, Expanded Abstracts, 553–556.

———, 2003, Shaded relief seismic attribute: Geophysics, **68**, 1281–1285.

Bednar, J. B., 1998, Least-squares dip and coherency attributes: The Leading Edge, **17**, 775–776.

Blumentritt, C. H., E. C. Sullivan, and K. J.Marfurt, 2003, Channel detection using seismic attributes on the Central basin platform, West Texas: 73rd Annual International Meeting, SEG, Expanded Abstracts, 466–469.

Claerbout, J. F., 1992, Earth soundings analysis: Processing versus inversion: Blackwell Scientific Publications.

Dalley, R. M., E. E. A. Gevers, G. M. Stampli, D. J. Davies, C. N. Gastaldi, P. R. Ruijetnberg, and G. J. D. Vermeer, 1989, Dip and azimuth displays for 3D seismic interpretation: First Break, **7**, 86–95.

Done, W. J., 1999, Removal of interference patterns in seismic gathers, *in* R. L. Kirlin and W. J. Done, eds., Covariance analysis for seismic signal process: SEG, 185–225.

Duncan, W., P. Constance, and K. Marfurt, 2002, Comparison of 3D edge detection seismic attributes to Vinton Dome, Louisiana: 72nd Annual International Meeting, SEG, Expanded Abstracts, 577–580.

Finn, C. J., 1986, Estimation of three dimensional dip and curvature from re-

flection seismic data: M.S. thesis, University of Texas at Austin.
Gersztenkorn, A., and K. J. Marfurt, 1999, Eigenstructure based coherence computations as an aid to 3D structural and stratigraphic mapping: Geophysics, **64**, 1468–1479.
Hart, B. S., R. Pearson, and G. C. Rawling, 2002, 3D seismic horizon-based approaches to fracture-swarm sweet spot definition in tight-gas reservoirs: The Leading Edge, **21**, 28–35.
Hesthammer, J., and H. Fossen, 1997, The influence of seismic noise in structural interpretation of seismic attribute maps: First Break, 15, 209–219.
Hill, S., M. Shultz, and J. Brewer, 1999, Acquisition footprint and fold-of-stack plots: The Leading Edge, **18**, 686–695.
Hoecker, C., and G. Fehmers, 2002, Fast structural interpretation with structure-oriented filtering: The Leading Edge, **21**, 238–243.
Kuwahara, M., K. Hachimura, S. Eiho, and M. Kinoshita, 1976, Digital processing of biomedical images: Plenum Press, 187–203.
Lin, M. I.-C., K. J. Marfurt, and O. Johnson, 2003, Mapping 3D multiattribute data into HLS color space — Applications to Vinton Dome, LA: 73rd Annual International Meeting, SEG, Expanded Abstracts, 1728–1731.
Liner, C., C.-F. Li, A. Gerztenkorn, and J. Smythe, 2004, SPICE: A new general seismic attribute: 72nd Annual International Meeting, SEG, Expanded Abstracts, 433–436.
Lisle, R. J., 1994, Detection of zones of abnormal strains in structures using Gaussian curvature analysis: AAPG Bulletin, **79**, 1811–1819.
Luo, Y., S. al-Dossary, and M. Marhoon, 2001, Generalized Hilbert transform and its application in geophysics: 71st Annual International Meeting, SEG, Expanded Abstracts, 1835–1838.
——–, 2002, Edge-preserving smoothing and applications: The Leading Edge, **21**, 136–158.
Luo, Y., W. G. Higgs, and W. S. Kowalik, 1996, Edge detection and stratigraphic analysis using 3D seismic data: 66th Annual International Meeting, SEG, Expanded Abstracts, 324–327.
Marfurt, K. J., and R. L. Kirlin, 2000, 3D broadband estimates of reflector dip and amplitude: Geophysics, **65**, 304–320.
Marfurt, K. J., R. L. Kirlin, S. H. Farmer, and M. S. Bahorich, 1998, 3D seismic attributes using a running window semblance-based algorithm: Geophysics, **63**, 1150–1165.
Marfurt, K. J., V. Sudhakar, A. Gersztenkorn, K. D. Crawford, and S. E. Nissen, 1999, Coherency calculations in the presence of structural dip: Geophysics **64**, 104–111.
Picou, C., and R. Utzmann, 1962, La coupe sismique vectorielle: Un pointé semi-automatique: Geophysical Prospecting, **4**, 497–516.
Roberts, A., 2001, Curvature attributes and their application to 3D interpreted horizons: First Break, 19, 85–100.
Scheuer, T. E., and D. W. Oldenberg, 1988, Local phase velocity from complex seismic data: Geophysics, **53**, 1503–1511.
Sullivan, E. C., K. J. Marfurt, and M. Ammerman, 2003, Bottoms up karst: New 3D seismic attributes shed light on the Ellenberger (Ordovician) carbonates in the Fort Worth basin (north Texas, USA): 73rd Annual International Meeting, SEG, Expanded Abstracts, 482–485.
Taner, M. T., F. Koehler, and R. E. Sheriff, 1979, Complex seismic trace analysis: Geophysics, **44**, 1041–1063.